†Electronic Supplementary Information

High-Performance Silicon-Based n-i-p Heterojunction Photoanode for Efficient Photoelectrochemical Water Splitting: Fabrication, Optimization, and Large-Scale Application

Kumar Shubham[1,2], Mukhesh K. Ganesha[1,3], Hafis Hakkeem[1], Athira Chandran M[1,3], A. Soundarya Mary[1], Anitesh Anand[4], Debasis De[4], Debasish Sarkar[5], Gobinda Gopal Khan[6] and **Ashutosh K. Singh*[,1,2,3]**

[1]*Centre for Nano and Soft Matter Sciences, Bangalore, Karnataka, 562162 India*

[2]Academy of Scientific and Innovative Research (AcSIR), Ghaziabad- 201002, India.

[3]*Manipal Academy of Higher Education, Manipal, Karnataka, 576104, India*

[4]*Energy Institute, Bengaluru, (Centre of Rajiv Gandhi Institute of Petroleum Technology), STRR, NH-648, Kamblipura, Hoskote, Bengaluru, Karnataka, 562114 India*

[5]*Department of Physics, Malaviya National Institute of Technology Jaipur, Rajasthan 302 017, India*

[6] *Department of Material Science and Engineering, Tripura University (A Central University), Suryamaninagar, Agartala, Tripura 799 022, India*

*Corresponding author and e-mail addresses: Dr. Ashutosh K. Singh (aksingh@cens.res.in, ashuvishen@gmail.com)

† Electronic supplementary information (ESI) available. See DOI: https://doi.org/….

Optimization O1: Thickness optimization of the Si layer

Fig. S1a† shows the variation of Si film thickness with deposition time over the optimized TiO_2 layer measured by a surface stylus profilometer. Fig. S1 (b), (c), (d), and (e)† show the top surface and cross-sectional morphology of the as-prepared photoanodes with and without annealing, respectively. It can be observed that, thermal annealing makes the TiO_2 and Si interface more compact and mixes well with each other. The adaptive interface mechanism is an efficient approach to prevent photocurrent loss caused by thermodynamic losses. The GIXRD pattern (Fig. S1f†) shows the improvement in the crystallinity of photoanodes after annealing. This enhancement in crystallinity, along with the development of a defect-free interface, is expected to facilitate the transport of photogenerated charge carriers between layers by reducing obstacles, thereby promoting more efficient charge transfer across the heterojunctions. These improvements are critical for achieving high-performance photoelectrochemical (PEC) activity.

PEC measurements were performed for four samples of different Si thicknesses to assess their performance. Fig. S2a† represents the photocurrent density vs time plot under On-Off cycles of light, the FTO/TiO_2/Si_A (0.5 hr) film with the lowest Si thickness, i.e., ~ 50 nm, gives the best photocurrent density of ~100 μA/cm^2, which is ten times higher than the other photoanodes tested. Similarly, the linear sweep voltammetry (LSV) curve (Fig. S2b†) under illuminated conditions mirrors these results, where the FTO/TiO_2/Si_A (0.5 hr) photoanode exhibited the highest photocurrent density of 90.2 μA/cm^2 at 1.23 V_{RHE} and other photoanodes FTO/TiO_2/Si_A (1 hr), FTO/TiO_2/Si_A (1.5 hr) and FTO/TiO_2/Si_A (2 hr) are showing photocurrent density values of 58.1, 53.8, and 32.2 μA/cm^2 at 1.23 V_{RHE}, respectively. These results suggest that as the thickness of the Si layer increases, the photocurrent density decreases. This decline can be attributed to the thicker Si films hindering the efficient movement of photogenerated carriers toward the TiO_2 conduction band, leading to charge recombination in the bulk Si. However, from the UV-vis-NIR absorption spectra (Fig. S2c†), it is evident that the increased Si thickness enhances light absorption in the visible range. This suggests two competing phenomena: i) thicker Si layers absorb more light, generating more photogenerated charge carriers and ii) the increased thickness also impedes charge transport, resulting in lower PEC performance due to carrier recombination as the film thickness increases. Given its best PEC performance, the FTO/TiO_2/Si_A (0.5 hr) photoanode was considered for further studies to prepare the *n-i-p* type FTO/TiO_2/Si/NiO photoanode.

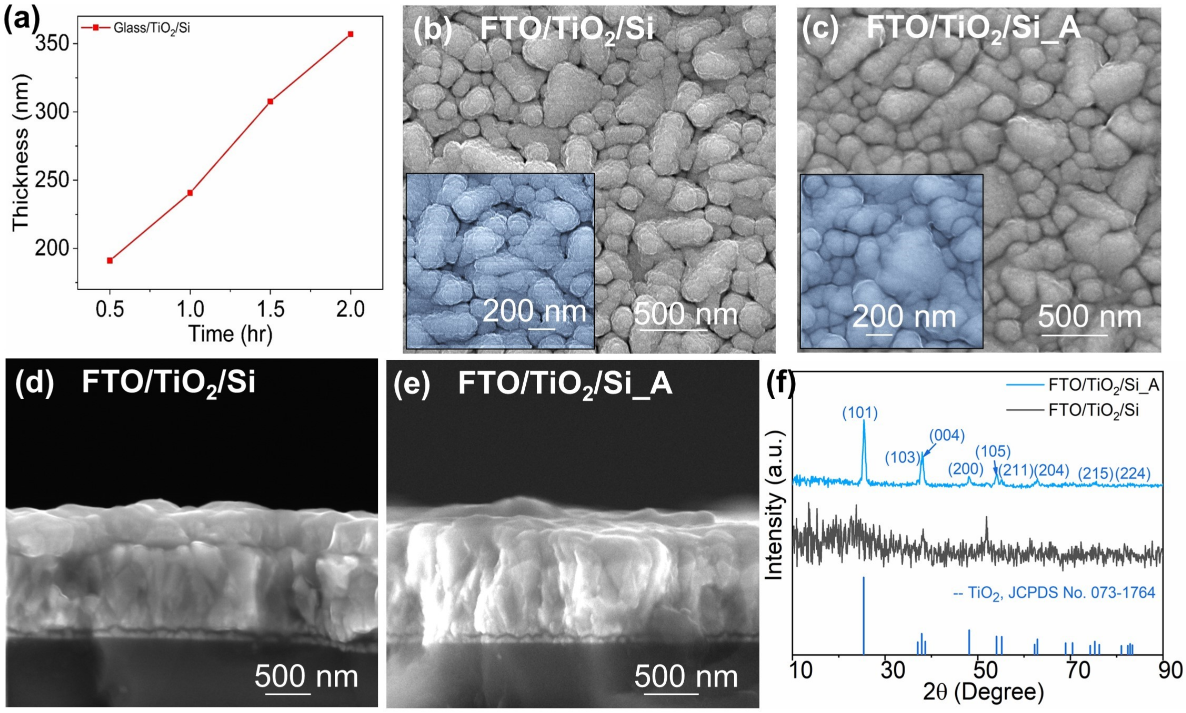

Fig. S1 (a) Thickness variation of Si layer with deposition time. Top surface FESEM images of (b) FTO/TiO_2/Si, (c) FTO/TiO_2/Si_A samples (insets are high magnification images of the surface showing nano globules). Cross-sectional FESEM images of (d) FTO/TiO_2/Si, (e) FTO/TiO_2/Si_A samples. (f) GIXRD pattern of the samples.

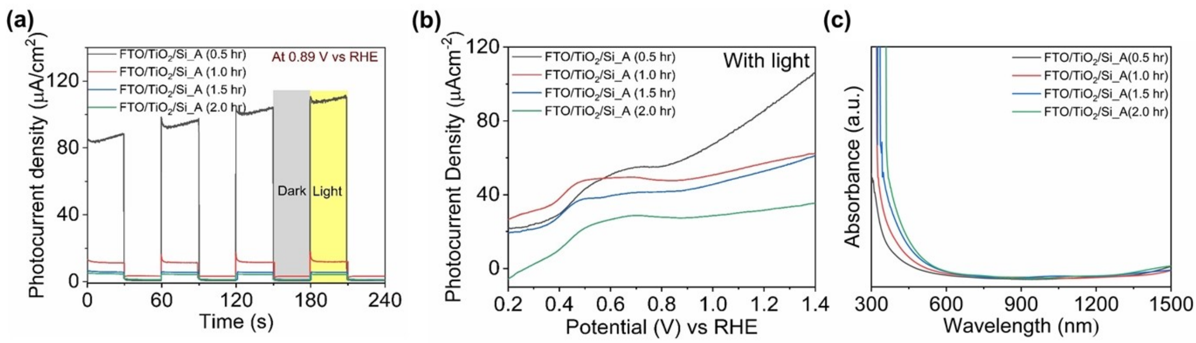

Fig. S2 (a) Chronoamperometric J-t curves of the photo-electrodes under light on-off cycles. (b) Photocurrent density vs. applied potential (*J–V*) curves under light conditions. (c) UV-vis-NIR absorption spectra of different photoanodes with various thicknesses of the Si-layer.

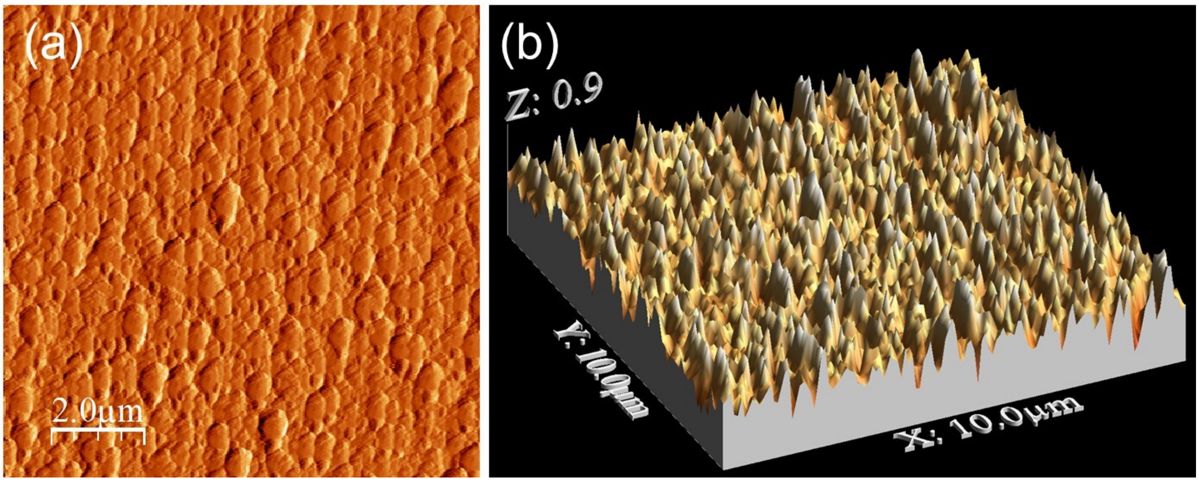

Fig. S3 AFM images of FTO/TiO_2/Si/NiO_A photoanode (a) 2D top view, (b) 3D topology.

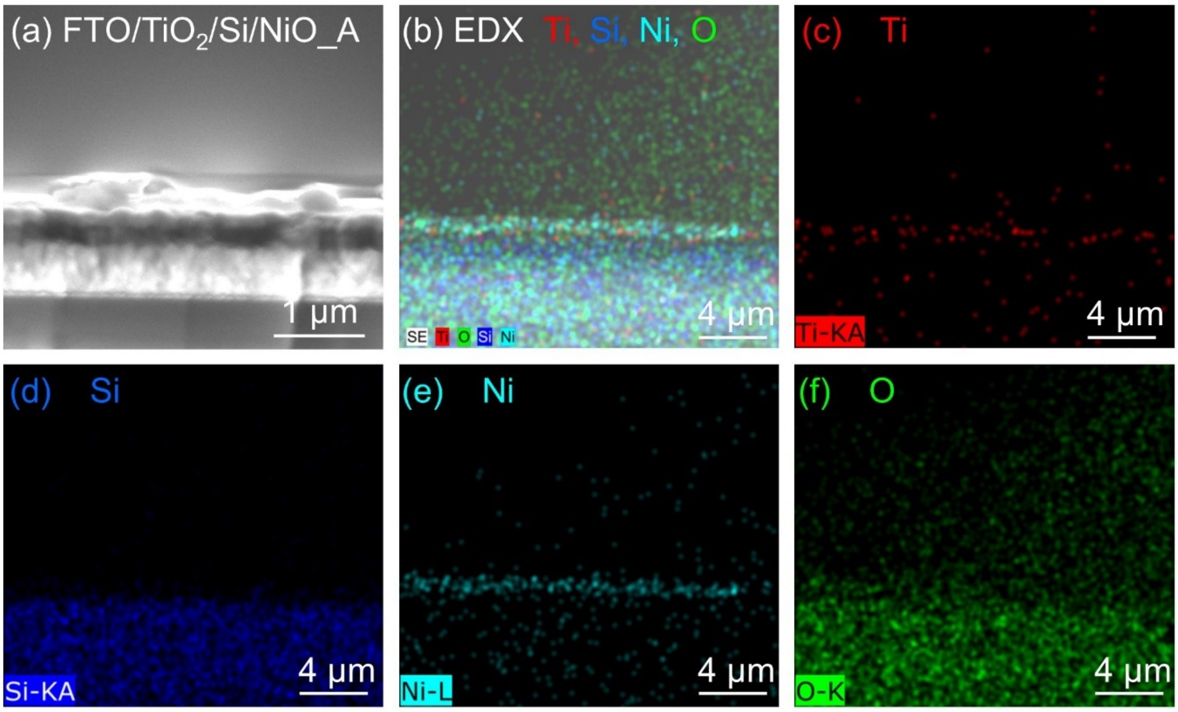

Fig. S4 Cross-sectional FESEM image of FTO/TiO_2/Si/NiO_A (a) and corresponding EDX color mapping of the heterojunction (b). EDX elemental color mapping for Ti (c), Si (d), Ni (e), and O (f).

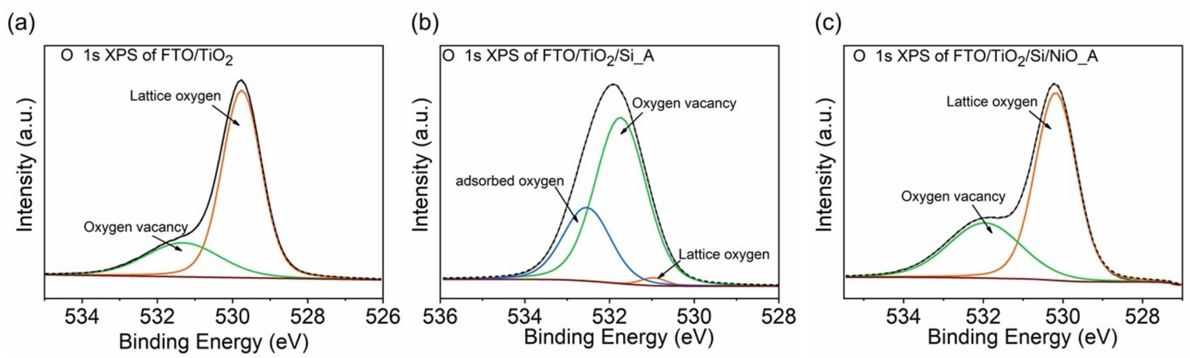

Fig. S5 High-resolution XPS spectrum of O 1s of (a) FTO/TiO_2, (b) $FTO/TiO_2/Si\_A$, and (c) $FTO/TiO_2/Si/NiO\_A$ photoanodes

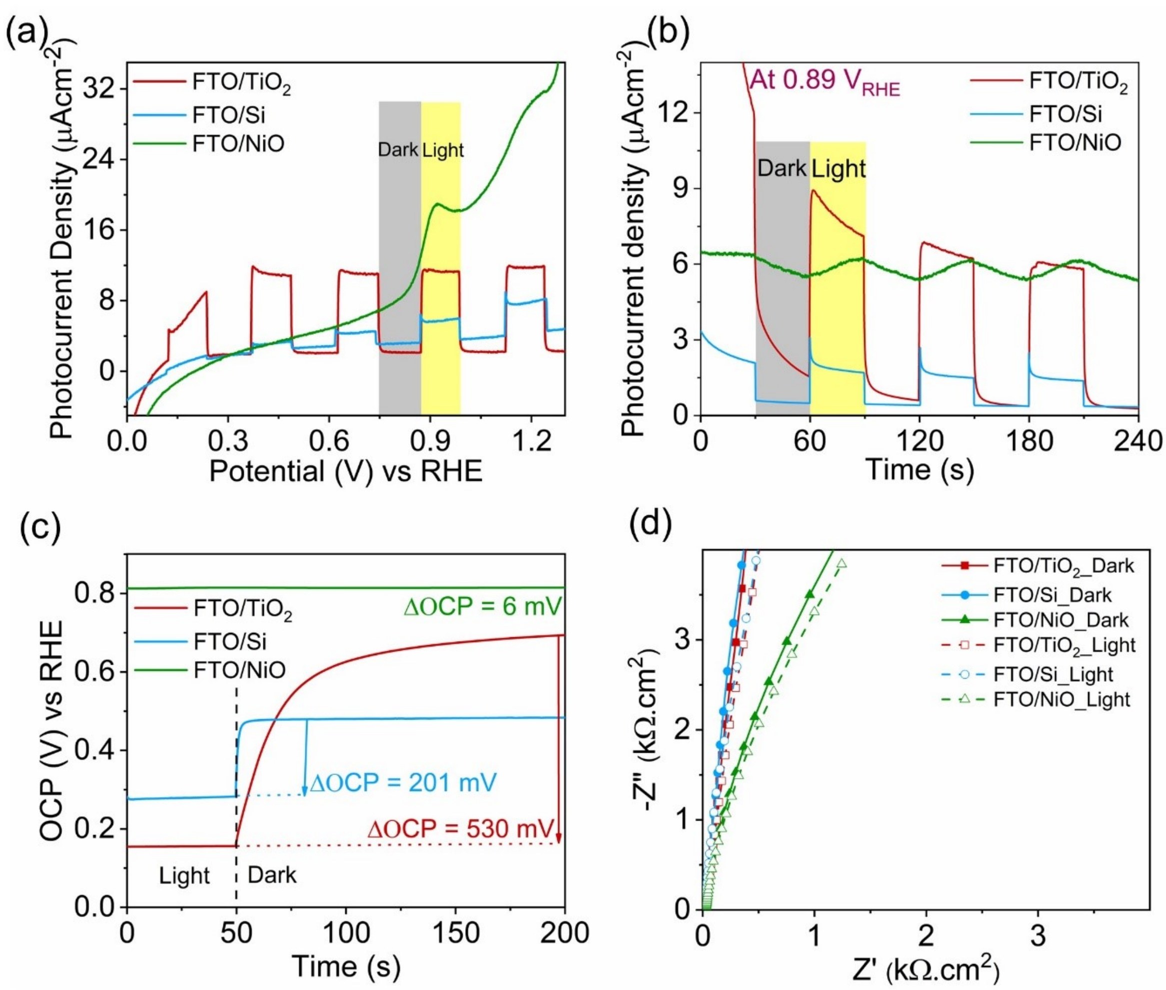

Fig. S6 Photoelectrochemical property measurement of individual TiO_2, Si, and NiO thin films. (a) LSV curves under chopped light illumination, (b) Chronoamperometric measurement at 0.89 V_{RHE} under light on-off cycle, (c) OCP vs. time plot in light and dark conditions, and (d) Nyquist plot under light and dark conditions of FTO/TiO_2, FTO/Si, and FTO/NiO Photoanodes.

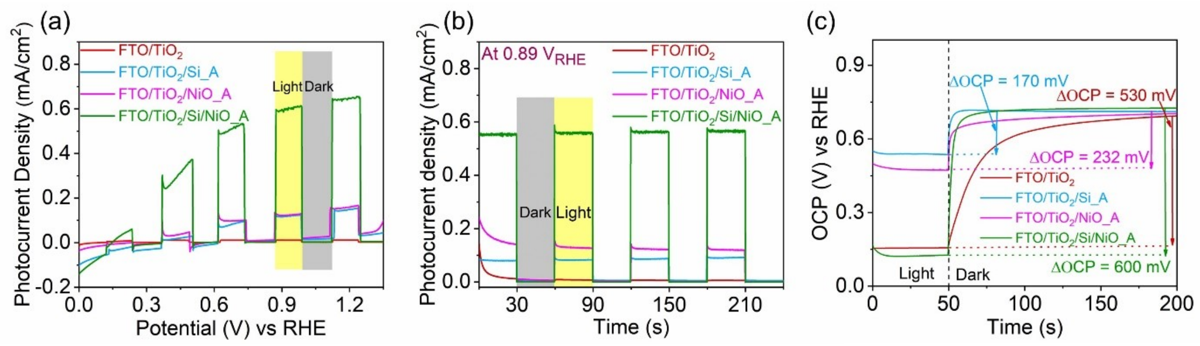

Fig. S7 PEC performance comparison of photoanodes with FTO/TiO_2/NiO_A photoanode where Si layer is not present (a) LSV curve under chopped light illumination, (b) Chronoamperometric measurement at 0.89 V_{RHE} under light on-off cycle, and (c) OCP vs. time plots in light and dark conditions.

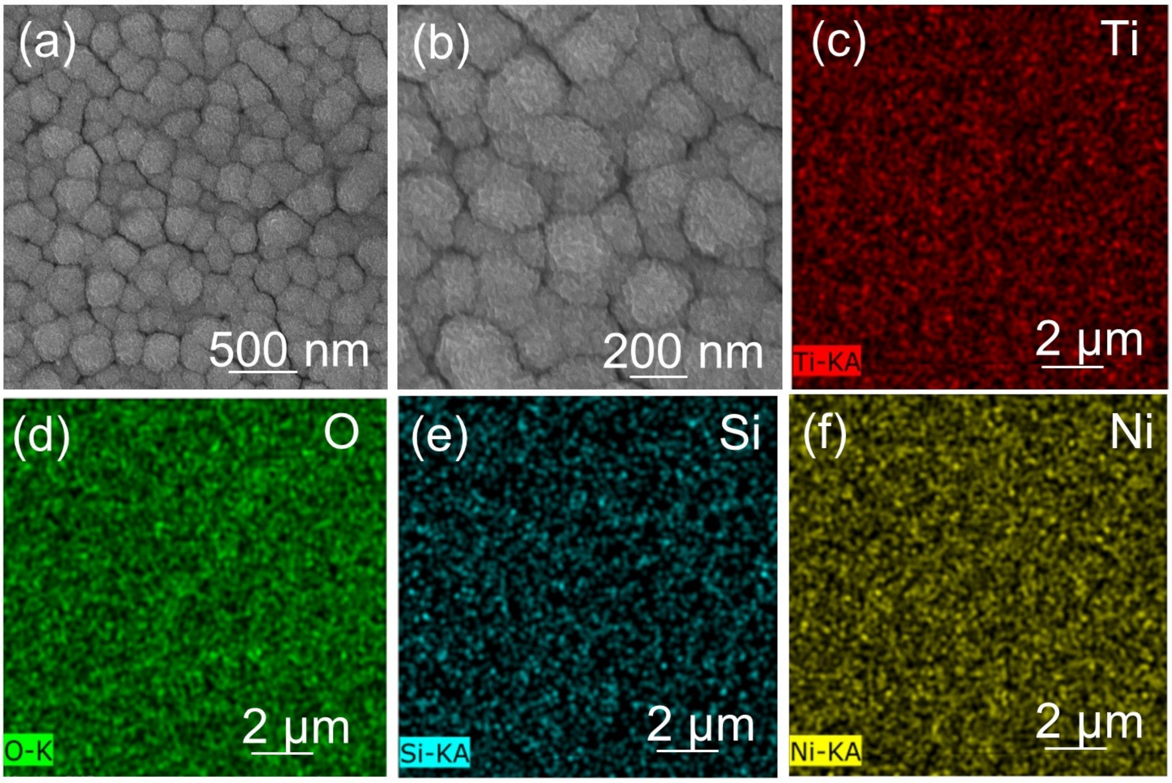

Fig. S8 (a, b) FESEM images of FTO/TiO_2/Si/NiO_A photoanodes after 10 hr stability test, (c-f) EDX color mapping of the elements present.

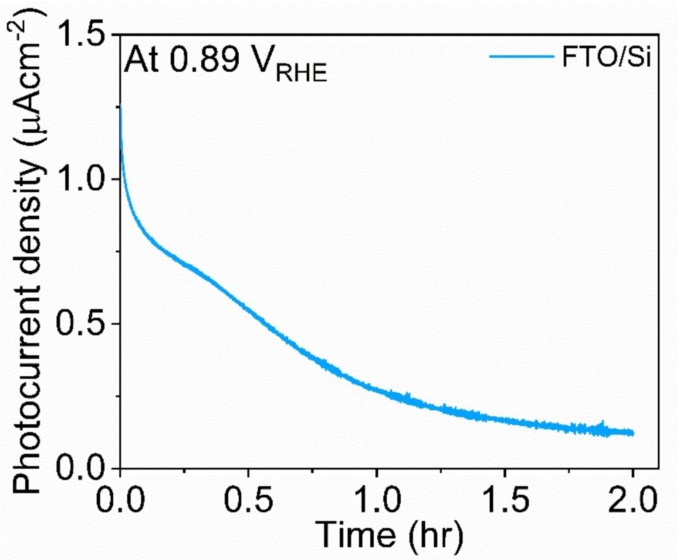

Fig. S9 Stability test of FTO/Si photoanode under 1 M KOH solution.

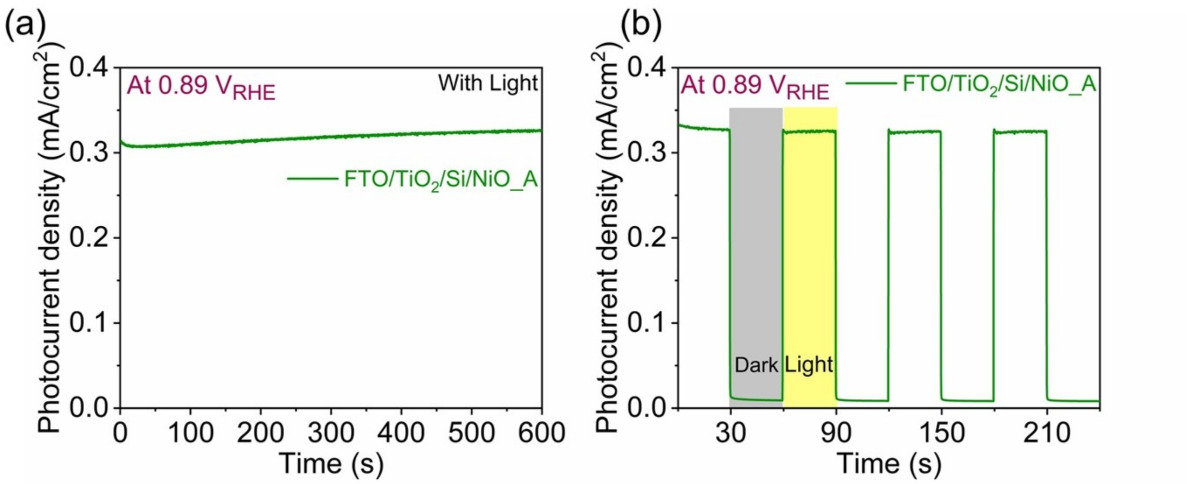

Fig. S10 Photoelectrochemical measurements of large area (~5 × 5 cm^2) FTO/TiO_2/Si/NiO_A photoanode (a) Chronoamperometric test for 600 s under light exposure, for video recording. (b) Chronoamperometric *J–t* curve of photoanode under light on-off cycles.

Table S1. XPS Peak fitting parameters for photoanodes:

Photoanode	Assigned	Peak position Binding energy (eV)	Area %
FTO/TiO_2	Ti $2p_{3/2}$	458.29	66.19
	Ti $2p_{1/2}$	463.98	33.81
	O1s Lattice oxygen	529.76	73.91
	Oxygen vacancy	531.32	26.09

FTO/TiO_2/Si_A	Si^0 $2p_{3/2}$ Si^0 $2p_{1/2}$ Si-O-C SiO_x	99.17 100.03 101.59 102.84	26.23 25.32 30.71 17.74
	O1s Lattice oxygen Oxygen vacancy Adsorbed oxygen	530.96 531.74 532.54	1.67 69.56 28.77
FTO/TiO_2/Si/NiO_A	Ni^0 Ni^{2+} Ni^{3+} Satellite peak 1 Satellite peak 2 Satellite peak 3	852.39 853.94 856.10 861.12 864.25 858.49	15.42 29.48 29.68 22.97 0.52 1.93
	O1s Lattice oxygen Oxygen vacancy	530.19 531.98	65.43 34.57

Table S2. Comparison of PEC performance with the other reported literature:

Photoanode	**Deposition Technique**	**Electrolyte**	**Photo voltage (mV)**	**Onset potential (V_{RHE})**	**Stability**	**Ref.**
GaN NWs/GaN buffer layer/Si	HCVD	NaOH		-0.26	>600 s	[1]
$TiN/TiO_2/Al_2O_3$	DC sputtering	Sewage water			1000 s	[2]
NiO_x/Ni/n-Si	Electro-Deposition	1 M NaOH	500	1.08	10000 s	[3]
np+-$Si/TiO_2/Co(OH)_2$	ALD, Electro-deposition	1 M NaOH	490	1.16	4 hr	[4]
n-Si/Graphene/TiO_2 / FeNiCoOx	APCVD, ALD, Electro-deposition	1 M NaOH	420	1	>6 hr	[5]
Ni/n-Si	e-beam evaporator	1 M KOH		~1.30	8 hr	[6]
CoVO/p+n-Si	magnetron sputtering	1 M KOH	608	1	3 hr	[7]
NiFe LDH/CoOx/n-Si	ALD, Electro-deposition	1 M KOH	171	0.95	6000s	[8]
$NiMoO_4/TiO_2$/Si nanowire	ALD, Hydrothermal	0.25 M KOH		0.85	600s	[9]
FTO/TiO_2/Si/NiO_A	magnetron sputtering	1 M KOH	600	0.11	> 10 hr	This work

References

1 N. Anbarasan, S. Sadhasivam, M. Mukilan and K. Jeganathan, *Nanotechnology*, 2020, **31**.

2 A. Almohammedi, M. Shaban, H. Mostafa and M. Rabia, *Nanomaterials*, 2021, **11**.

3 S. A. Lee, T. H. Lee, C. Kim, M. G. Lee, M. J. Choi, H. Park, S. Choi, J. Oh and H. W. Jang, *ACS Catal.*, 2018, **8**, 7261–7269.

4 Y. Yu, Z. Zhang, X. Yin, A. Kvit, Q. Liao, Z. Kang, X. Yan, Y. Zhang and X. Wang, *Nat. Energy*, 2017, **2**.

5 C. Li, Y. Xiao, L. Zhang, Y. Li, J. J. Delaunay and H. Zhu, *Sustain. Energy Fuels*, 2018, **2**, 663–672.

6 S. Li, G. She, C. Chen, S. Zhang, L. Mu, X. Guo and W. Shi, *ACS Appl. Mater. Interfaces*, 2018, **10**, 8594–8598.

7 Z. Xing, H. Wu, L. Wu, X. Wang, H. Zhong, F. Li, J. Shi, D. Song, W. Xiao, C. Jiang and F. Ren, *J. Mater. Chem. A*, 2018, **6**, 21167–21177.

8 Z. Chen, K. Fang, Y. Bu and J. P. Ao, *J. Alloys Compd.*, 2023, 942.

9 F. Wu, Q. Liao, F. Cao, L. Li and Y. Zhang, *Nano Energy*, 2017, **34**, 8–14.